Erschienen in: Solar Energy Materials and Solar Cells ; 120 (2014). - S. 275-281
https://dx.doi.org/10.1016/j.solmat.2013.09.018

On the origin and formation of large defect clusters in multicrystalline silicon solar cells

Dietmar Kohler*, Annika Zuschlag, Giso Hahn

University of Konstanz, Department of Physics, P.O. Box X916, 78457 Konstanz, Germany

ARTICLE INFO

Keywords:
Multicrystalline silicon
Solar cell
Defect cluster
Luminescence
Crystal orientation
Raman

ABSTRACT

Large defect clusters can represent a serious reduction of the material quality of multicrystalline silicon and the efficiency of the resulting solar cells. It is useful to find the origin of these defect rich regions in order to understand their formations. For this work, multicrystalline silicon wafers from different positions of a compensated p type silicon brick were processed to solar cells with a homogeneous emitter and screen printed metallization. The solar cells from the main part of the brick showed efficiencies between 15.6% and 16.1%. The characterization for this work focuses on the positions of the three largest defect clusters by means of detailed optical, crystal orientation and electrical loss measurements. This allows the localization of the defect clusters' origins during crystallization. The locations where the observed defect clusters started to grow, show similar crystal configurations. This implies that the large clusters formed preferentially at grain boundaries between specific grain orientations. A smaller cluster disappeared at a grain boundary. The characterization showed the same crystal configuration as for the three large growing clusters.

1. Introduction

Defect clusters are local accumulations of crystal defects like grain boundaries and especially dislocations. They can heavily decrease the material quality by drastically reducing the diffusion length of minority charge carriers. The influence of dislocations on the material quality and on solar cells depends on several factors, e.g. their decoration with impurities [1 4]. The reduction of the diffusion length for an increasing dislocation density was modeled by Donolato [5]. On the basis of Donolato's work, Kieliba et al. [6] studied the decrease of the open circuit voltage V_{oc} for increasing dislocation densities. In an earlier work, we showed that this applies also for defect clusters [7]. Experiments on small solar cells have been presented, which were cut out of large area cells that included extended defect clusters. The small cells that contained defect clusters showed lower V_{oc} and lower short circuit current densites j_{sc} than dislocation free solar cells. These effects were caused by defect clusters as well as by large networks of disloca tions. Haunschild et al. [8] presented a direct correlation between V_{oc} and the fraction of crystal defects, which had been calculated from photoluminescence (PL) images.

Dislocations are typically caused by stresses within the crystal. These can be mechanical or thermal gradients occurring during crystallization of the ingot or during processing. Häßler et al. [9] stated from numerical simulations that the dislocation density during crystallization follows three phases. A first strong disloca tion generation right after the solidification is expected. This is followed by a dislocation multiplication during cooling down to 600 °C. Below this temperature, the dislocation multiplication stops. Usami et al. [10] concluded from their comparisons of shear stress calculations with dislocation density measurements that the dislocation densities in multicrystalline silicon are related to the shear stresses around grain boundaries. On the other hand, it also seems to be possible to reduce dislocations by small stresses. Hartman et al. [11] observed significant decreases of the disloca tion densities in SiN_x coated String Ribbon multicrystalline silicon wafers that were annealed at temperatures of up to 1366 °C for 6 h. According to works of Di Sabatino and Stokkan, it is also possible to achieve higher grain sizes as well as preferred grain orientations for increased initial ingot cooling rates [12].

Grain boundaries between two neighboring grains can be classified according to the crystal configurations and symmetries. Boundaries of grains that share a regular part of their atoms, are called coincidence site lattice (CSL) boundaries. They are classified by Σ, which is the reciprocal density of coincidence sites. Bound aries with high symmetries appear more often due to lower formation energies. CSL boundaries with increased degrees of symmetry are twin boundaries. The highest fraction of common atoms represents Σ3 grain boundaries where every third atom is part of both crystal grains. Examples for different twin boundaries will be presented in the results.

This present work has the purpose to focus on the origin and the formation of similar large defect clusters. Several hundred wafers from the same brick were available for this experiment.

* Corresponding author. Tel.: +49 7531 88 3174; fax: +49 7531 88 3895.
E-mail address: dietmar.kohler@uni-konstanz.de (D. Kohler).

Konstanzer Online-Publikations-System (KOPS)
URL: http://nbn-resolving.de/urn:nbn:de:bsz:352-252467

Some of the wafers were processed to solar cells and were measured using a forward biased electroluminescence (EL) setup. This enables us to identify the lateral and vertical positions of several clusters' origins. This information can be used for detailed measurements at these sections. The parts of neighboring wafers that contain the cluster formation areas were cut into 2×2 cm^2 pieces. After a polishing etch, the positions of the cluster origins were scanned using the EBSD (electron backscatter diffraction) mode of a scanning electron microscope (SEM) to receive information about the crystal orientation. From the crystal orientation of two neighboring grains, the grain boundary types can be calculated if the boundaries are specific CSL boundaries.

Other neighboring wafers were etched in a grain selective or a dislocation selective solution. The etched wafers were investigated with an optical microscope or scanned using an optical scanner setup to receive optical information about the crystal structure and the dislocation formations. This allows to investigate and to compare the crystal structures at the origins of the largest defect clusters.

2. Materials and experiment

The studied material was part of the center brick of a compensated p type multicrystalline silicon ingot that was sawn into 25 bricks. Compensated silicon typically contains higher concentrations of boron and phosphorus as dopants. This is due to the different cleaning process. Furthermore, the net dopant concentration must be adjusted by the addition of boron or phosphorus because it is related to the bulk resistivity. The increased density of impurity atoms represents point defects that can also lead to higher dislocation densities. This may result in more defect clusters. These defects are not limited to compensated silicon, but are also well known in uncompensated multicrystalline silicon from conventional cleaning processes. The occurence of dislocations can be reduced by an adjusted cooling rate during the crystallization process, but not avoided completely [13,14].

For this experiment, 12.5×12.5 cm^2 wafers with a thickness of approx. 190 μm have been used. The wafers were taken from different heights of the same brick. All wafers from the wafered p type part were numbered from the bottom to the top. These numbers are in the following indicated by “#”. About half of the 500 wafers of this brick were available. 40 of these wafers were processed to solar cells with a homogeneous emitter formed by $POCl_3$ diffusion and screen printed firing through SiN_x metallization. In a first step, the entire areas of all processed solar cells were characterized with an EL setup under forward and reverse bias. For selected cluster containing parts of these solar cells, the spatially resolved internal quantum efficiency (IQE) was measured using light beam induced current (LBIC).

Neighboring wafers at these positions were either alkaline etched in order to enhance the reflection contrast between crystal grains of different orientations, or Secco etched [15] to reveal the dislocation structures. Further neighboring wafers at cluster containing areas were prepared for EBSD measurements. For that, the relevant sections were sawn out and chemical polishing (CP) etched with an etching solution based on hydrofluoric acid, acetic acid and nitric acid. The etched wafers were measured using a SEM with an included EBSD setup. Here, the sample is placed in an angle of 70°. Back scattered electrons at the crystal planes lead to Kikuchi diffraction patterns. These patterns offer information on the crystal symmetries and the relative angles in between the grains. The orientations of crystal grains as well as the grain boundary types can be calculated using this information [16,17]. The orientation maps are based on inverse pole figures (IPF). In the shown EBSD maps, they are superposed with the grain boundary type lines according to the CSL. Additionally, Raman measurements, which are related to local stresses, were taken at one significant wafer area with a Raman setup by WITec using a HeNe laser with a wavelength of 633 nm.

3. Results

In the following, the current voltage characteristic curves are shown in dependence of the ingot height. Then, we focus on the largest observed defect clusters in order to understand their formation mechanisms. Additionally, these results are compared to the opposite effect: a small defect cluster shrinks during the crystallization and is positioned in the opposite crystal configuration than the observed growing clusters.

3.1. Solar cell results

The solar cell results reveal typical limitations of compensated material. The current voltage (I V) characterization of the processed solar cells is shown in Fig. 1. The compensation of the segregating dopants leads to a decreasing net dopant concentration. This results in an increasing bulk resistivity towards the type inversion and limits V_{oc} as well as the efficiency. For an older material, we had observed an increasing j_{sc} in the upper part of the brick where the resistivity increases strongly [18]. We had assumed that the recombination losses at dopants might be reduced by the possible formation of B P pairs [19]. This was not observed for the new material, shown in Fig. 1 on the right. In

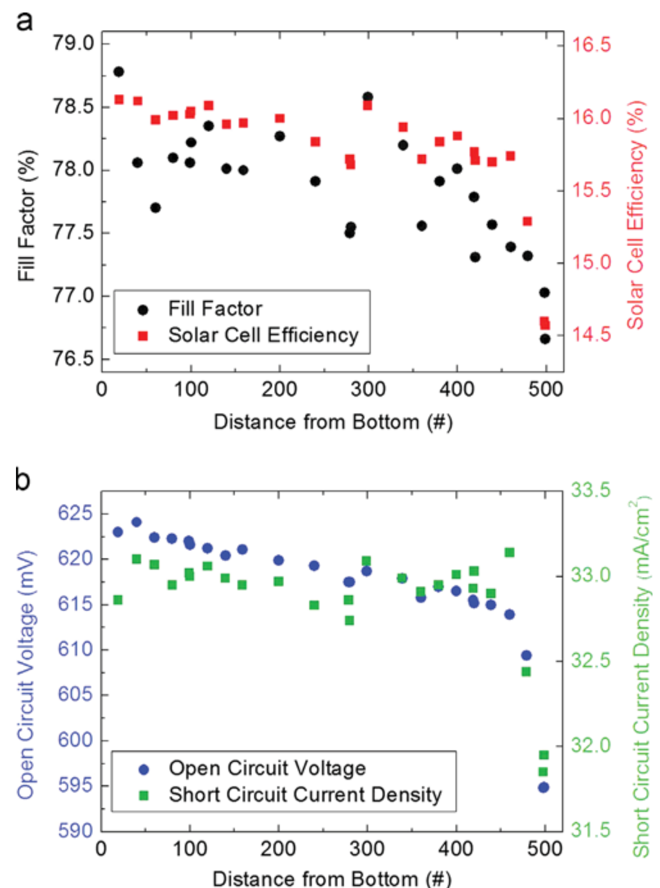

Fig. 1. I–V characterization in dependence of the distance from the position of the lowest wafer in the block according to the wafer number. The segregation and compensation of the dopants boron and phosphorus limit V_{oc}. In the upper part, j_{sc} decreases, probably due to losses that are caused by the high impurity concentrations. Minor problems in the solar cell process lead to the relatively strong scatter of the fill factor.

contrast, the j_{sc} remains stable at a higher level of about 33 mA/cm^2 until it decreases in the upper part of the brick. The stronger decrease can be explained with the higher positioned type inver sion that leads to higher concentrations of segregated impurities e. g. metals at this point.

3.2. Origin and formation of defect clusters

This work focuses on the formation of three large defect clusters that developed within the available multicrystalline sili con brick. The first step is represented by the localization of the clusters' origins. At these positions, detailed space resolved mea surements are executed to learn more about possible reasons for the clustering of these large defect structures. The characterization of solar cells with an EL setup offers a fast and easy possibility to obtain information about the non radiative recombination active defects in the material. This allowed to trace back the clusters by comparing the images downwards until the defect clusters were no longer visible. Fig. 2 shows the growth of the investigated large defect clusters. On the left, the three largest defect clusters are visible in the EL image of the solar cell from position #419. The very low luminescence intensity is caused by increased recombi nation losses due to high dislocation and grain boundary densities. For each of these marked growing clusters, three steps for increasing vertical positions are shown on the right. The marks indicate the positions of the evolving clusters. The three clusters were chosen according to their visible sizes. Concerning the recombination active parts, all three clusters exceed horizontal dimensions of 1 cm^2 and reach sizes of up to several cm^2. Additional PL measurements on SiN_x:H passivated wafers also confirm strong decreases in the minority charge carrier lifetimes for the defect cluster areas compared to cluster free wafer parts.

Considering the formation of cluster A as shown in Fig. 2, this cluster already starts to grow close to the bottom of the ingot. The localization of the starting point is difficult at the lowest measured position because the luminescence intensity of the whole wafer is low. The forming cluster is clearly visible in the EL image of the solar cell #159 in Fig. 3 on the left. The cluster parts seem to be connected to a large grain boundary that can be seen below the cluster. The EBSD measurement in Fig. 3 shows only few grain boundaries in the area of the cluster, although the cluster lines are visible in EL within several neighboring wafers. This means that these lines are probably small angle grain boundaries, which are lineages of dislocations. Judging from the high non radiative recombination losses, these dislocation lineages are decorated with impurities. Measurements on solar cells from higher positions show that the defect cluster in the (101) orientated grain is shifted away from the large (111) grain (in blue). This will be discussed later in detail with regard to the EBSD maps shown in Fig. 9. While the position of the origin of cluster A cannot be located exactly as the cluster started within the lowest part of the ingot, this becomes interesting for cluster B.

The detailed EL images in Fig. 2 for cluster B show two dark areas of rather large losses due to non radiative recombination at the height position #199, visible as two small defect clusters.

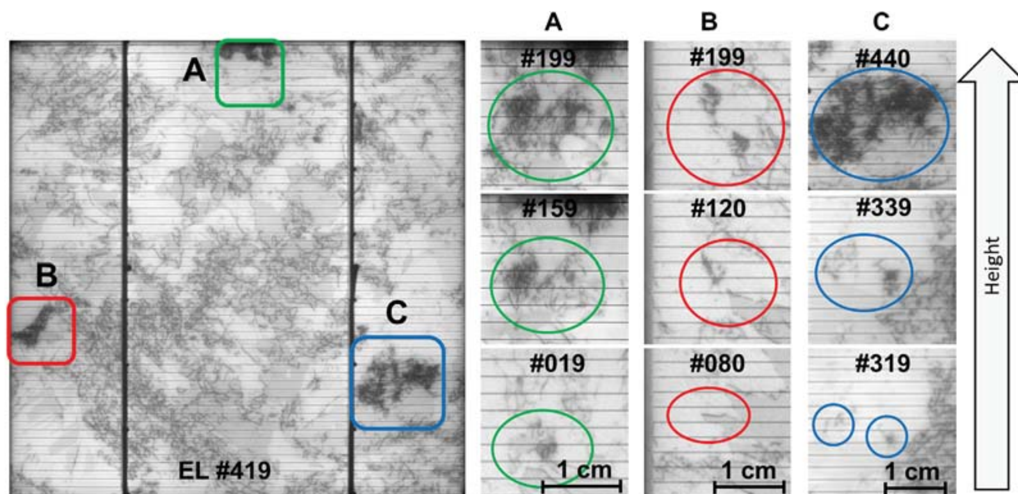

Fig. 2. The EL image under forward bias of the solar cell from position #419 (left) compares the positions within the center brick as well as the sizes of the three large defect clusters, which were focused on in this work. Detailed steps of these clusters' growth with ingot height are shown on the right.

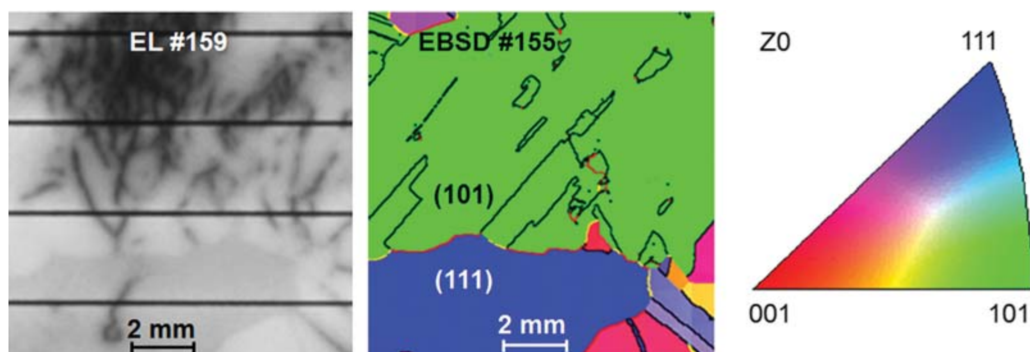

Fig. 3. The forward biased EL image of the solar cell #159 gives an impression of the growth of cluster A. The EBSD (IPF+CSL) measurement in the middle indicates that the defects grow in the (101) orientated grains (in green) at a grain boundary with the large (111) grain (in blue) beneath.The clustering already started at the bottom of the ingot. The defects seem to grow in contact with the large grain beneath. (For interpretation of the references to color in this figure legend, the reader is referred to the web version of this article.)

The location of the clusters' origin was determined by comparisons of EL and PL measurements on neighboring vertical positions. Both clusters seem to start very close to the left end of the recombination active grain boundary section that can be seen in Fig. 4. The EL image in the upper picture was measured under 10 mA/cm^2 forward bias (597 mV). The loss of the IQE in the lower picture at the same grain boundary section is significantly higher than for the other defect structures in the observed area. This is probably caused by the assumed high decoration with impurities.

In search for a better understanding of these clusters' formation, further detailed measurements were carried out at the left end of this grain boundary section (see Fig. 5).

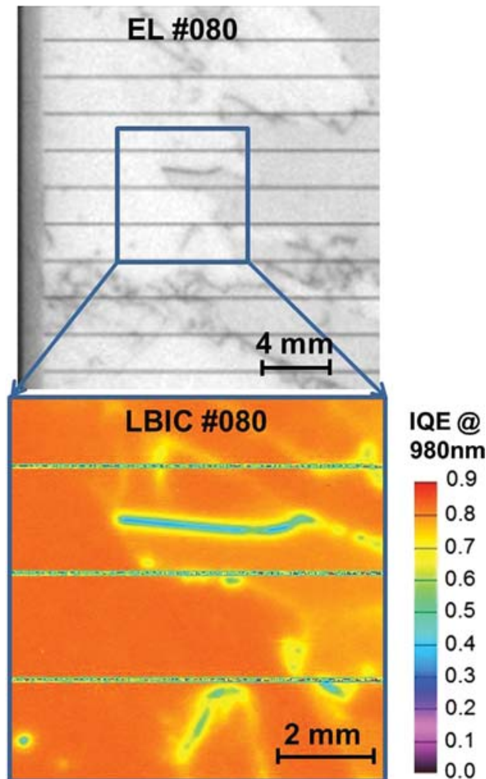

Fig. 4. The EL image under forward bias in the upper picture shows the position where the formation of cluster B started. According to the comparison of neighboring solar cell measurements, the cluster's orgin is situated on the left end of the recombination-active grain boundary section. This area is also clearly visible in the LBIC map of the IQE in the lower picture (horizontal stripes are caused by the front finger grid).

According to the optical scan of the grain selective etched wafer #076 and the EBSD results on #077, the origin's position is situated at the crossing of three grain structures. The EBSD measurements of this area show that the two left and upper grains both have an orientation in the range of (101) while the lower grain is (111) orientated. The information on the orientations of the neighboring grains allows to calculate the types of the enclosed grain boundaries. The two upper grains are indicated as Σ3 twin grains. The EBSD close up reveals even doubled Σ3 twin grain boundaries starting right at the tip of the (111) grain where the recombination active section in Fig. 4 ends. A model for the formation of these parallel (111) Σ3 twins was presented by Fujiwara et al. [20]. The optical microscope image of the grain selective etched wafer #076 in Fig. 5 on the right shows the narrow tip of the (111) grain where the doubled twins start.

As mentioned above, crystal stresses can lead to higher dislocation densities. Fig. 6 shows the results of a Raman measurement on the neighboring wafer #077. This wafer was chemically polished as described above in order to gain a rather smooth surface. Besides the usability for the EBSD measurement, this includes enough information to locate the grain boundaries without a higher etch rate at the grain boundaries. The structures visible in Fig. 6 on the left are formed by soft dents due to the specific chemical polishing. Many of these structures are aligned in dependence of the grain orientations and thereby indicate the locations of the grain boundaries. The Raman map on the right in Fig. 6 shows the shift of the Raman peak for each position. The vertical lines are related to the linear horizontal scanning and are caused by variations of the measurement setup e.g. of the laser or the temperature. The two bright dots within the upper right grain also appear in the optical image and are assumed to be caused by surface damages or impurities. They are not relevant in the context of this work. The black ellipse marks the area of the grain tip. There is a small bright spot where one of the twins starts at the large grain boundary. This positive frequency shift compared to the assumed relaxed silicon grain areas indicates compression concerning the wafer surface. In contrast, the dark section at the position where the grain boundary bends between the pairs of doubled twins indicates expansion. The expansion leads to tensile stresses that are expected to increase the occurance of dislocations. This might enable the observed formation of dislocation clusters at this location.

It is possible that the twins as well as the defect clusters are both related to the present (101) grain orientation. A second small defect cluster is formed at the same location about 40 wafers higher. Similar effects were observed there. Detailed measurements for the third defect cluster C can be seen in Fig. 7. The LBIC

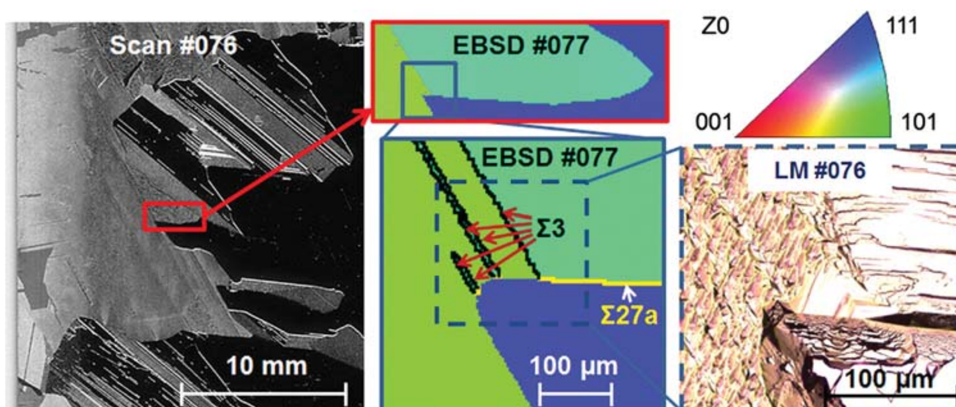

Fig. 5. Detailed measurements on the origin of cluster B. The optical scan of the grain-selective etched wafer #076 (left) and the EBSD measurements (middle) show the cluster's origin position at the crossing of three different grain orientations. Doubled Σ3 twin grain boundaries can be seen right at the left tip of the (111) grain where the recombination-active section in Fig. 4 ends. The optical image of the grain-selective etched wafer #076 (right) shows the tip of the (111) orientated grain.

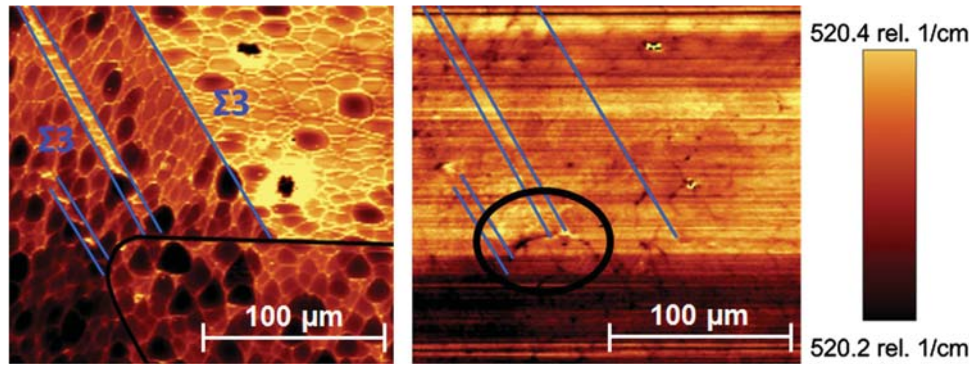

Fig. 6. The shown images result from a Raman measurement on the chemically polished wafer #077 and show the grain tip area from Fig. 5. The bend of the grain boundary as well as the twin boundaries are marked in the optical image (left). The Raman map (right) shows the frequency shifts of the Raman peak, which are related to mechanical stresses within the material. Especially the tensile stress (dark in marked area) at the bend of the boundary is expected to create increased dislocation densities. The vertical changes are probably caused by variations of the laser intensity and the temperature.

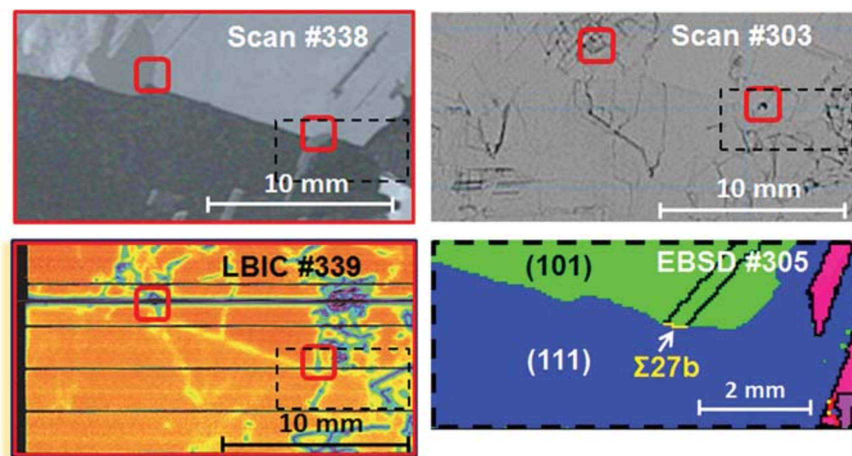

Fig. 7. The cluster C seems to start at least at two areas, which are indicated with the red squares in the grain-selective etched wafer scan (#338) and the LBIC measurement (#339). At the lower position #303, deeper etchings at these sites are observed. According to the EBSD measurement on #305, the orientations of the neighboring grains are (101) and (111), similar to the other observed cluster origin areas. The horizontal line visible in the LBIC picture was induced by a sawing line.

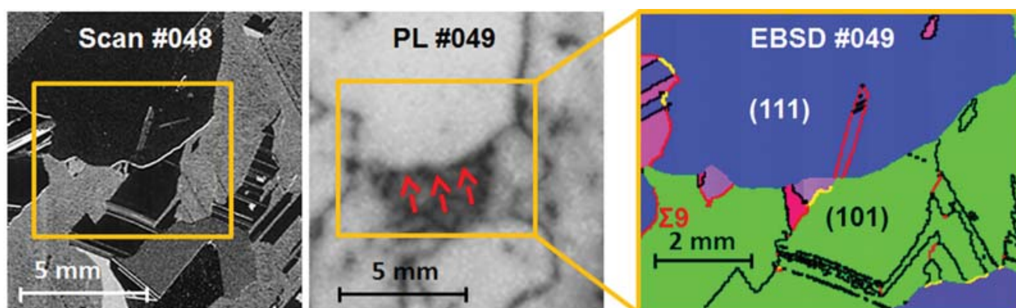

Fig. 8. A defect cluster, visible in the PL image in the middle, disappears at the grain boundary for increasing ingot height. The EBSD measurement shows that the neighboring grains are orientated in (101) and (111).

measurement of the solar cell from position #339 shows that the large cluster, which is shown in Fig. 2 for the position #440, starts at least at two different areas. The grain selectively etched wafer #338 shows that both of these marked areas are located close to and connected to a long grain boundary section. The formation of the cluster can be followed back to the lower position #303. This wafer was etched dislocation selectively and seems to show etched defects at the marked areas. This might indicate crystal deformations for the possible origins of the defect clustering, although the actual reason is unknown. More significant is the EBSD measurement of the neighboring wafer #305. This cluster is formed inside (101) grains close to a grain boundary with the neighboring (111) grain.

The comparison of the results for the clusters A, B, and C reveals that the crystal configuration is the same for all three observed large defect clusters, which were only selected according to their sizes. This will be discussed later.

3.3. A disappearing cluster

The defect clusters described above grow with increasing ingot height. It is also possible that defect clusters disappear again

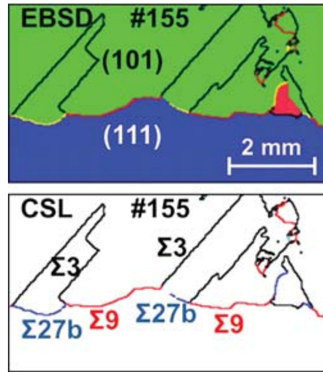

Fig. 9. The EBSD measurement at position #155 shows the area where cluster A seems to be connected to a large grain boundary (see also Fig. 3). The CSL types are indicated in the image on the right. The type of the large grain boundary line changes due to the alternating orientations of the twinned (101) grains.

during the crystal growth. This is the case for the defect cluster area shown in Fig. 8. The comparison of PL images of hydrogen passivated wafers from different positions implies that this cluster moves towards the large grain in the upper part of the image, as indicated by the red arrows, in relation to the shown position. There, the cluster disappears gradually at a contrast line with increasing height. The optical scan on the left was made on the grain selectively etched neighboring wafer #048. It reveals that this line is a large grain boundary. The crystal orientations in this section measured with EBSD are shown in Fig. 8 on the right. It can be seen that the defect cluster is present in the grains with (101) orientation. The optical scan shows that these grains in [101] directions, which are shown in green in the EBSD image, differ in their crystal angle. This difference is not visible in the shown EBSD image because the color reveals only the 2D projection of the orientation. Together with these grains, the cluster disappears at the grain boundary to the upper (111) orientated grain. The constellation of the crystal orientations is similar to those large clusters previously discussed: also in this case, the defect cluster is present in (101) grains. The (111) grain seems to be dominant over the (101) orientated grains with increasing ingot height.

4. Discussion

The shown clusters were chosen for the presented detailed investigations because their size exceeded a horizontal area of 1 cm^2. It seems significant that all three observed locations have several properties in common. All three observed large defect clusters formed very close to grain boundaries. It is plausible that the clusters start in contact with grain boundaries as it is well known that the stresses at certain grain boundaries tend to be reduced by dislocations [21,22]. The first cluster A formed close to the bottom of the ingot. It was concluded that the clusters can also be caused by the long neighboring grain boundary section. This is in accordance with published results e.g. by Odland and Stokkan [23]. Additionally, the grain boundaries for all three clusters are characterized by the crystal configuration. The clusters grow in grains with orientations equal or close to (101) while the neigh boring grains are (111) orientated. The (101) grains also contain especially Σ3 twin grain boundaries, while the (111) grains seem to be rather large and stable.

The crystal configuration for the disappearing cluster in Fig. 8 is similar. Here, the cluster is also present in (101) grains. This cluster disappears gradually for increasing ingot height because the (101) grains are shifted towards the (111) grain. The twinned (101) grains in the presented cluster areas are each colored in the same way except for #077 shown in Fig. 5. This is based on the fact that the coloring follows only the projection of the orientation. Thus, the resulting color code is axially symmetrical for rotations around this axis for grains with one axis exactly parallel to the projection axis [24]. In #077, the orientations differ from the exact directions and therefore are displayed in slightly different colors.

The CSLs of the grain boundaries between the (111) grain and the twinned (101) grains change for #077 between Σ=27a and Σ=9. The ⟨110⟩ Σ9 grain boundaries could not be visualized in the CSL image in Fig. 5. But the CSL can be derived by the misorienta tion angle of 38.87 ± 0.5° that was indicated for this boundary. This is consistent with the known value of 38.94° for ⟨110⟩ Σ9 [25]. The misorientation angle defines the minimum rotation angle between the two neighboring grains and is characteristic for the CSL grain types. The same observation was also made for the disappearing cluster in #049. The grain boundaries between the (111) grain and the (101) grains in Fig. 7 result in misorientation angles of about 38.79 ± 0.5°, which fits Σ9, and 31.45°, which fits Σ27a. The differentiation between the configurations Σ27a for #077 (Fig. 5) and Σ27b for the other exactly (111) (101) orientated boundaries is based on the different misorientation angles of 31.58° for Σ27a and 35.43° for Σ27b.

These considerations lead to the results that the cluster origins are situated in areas of twin crossings (Σ9 and Σ27 are higher order twins). These crossings are shown for the cluster A in Fig. 9. The effect of grains that are formed by Σ3 and higher order twins is commonly known as the *dissociation of grain boundaries* [26,27]. It seems that this configuration supports the formation of the observed large defect clusters. Additionally, the cluster shown in Fig. 8 disappears at the same grain boundary type. This dominance of the large grain can be explained by a higher stability during the crystal growth of the (111) grain compared to the (101) grains. The planes that are formed by Σ3 grain boundaries are often parallel to {111} crystal planes [28]. These are known to be slipping planes. In the present case, the {111} orientations refer to the direction that is vertical to the wafer surface, meaning that the {111} as well as the Σ3 planes are parallel to the crystallization front. This might explain why the observed {111} grains contain less grain boundaries and are more stable than the {101} grains. The stability is related to the boundary energy. The energy levels of the grain boundaries depend on their symmetries but also on their orientations relative to the crystals [26]. For crystallization rates below 30 μm/s (10.8 mm/h), the {111} orientated grains are expected to be dominant in multi crystalline silicon because of a higher growth rate, due to a lower interface energy [28 30].

5. Conclusion and outlook

Defect clusters can represent significant limitations for the efficiency potential of multicrystalline silicon solar cells. Here, we focused on the formation of the three largest defect clusters in the available brick from a compensated ingot. The clusters' origins were localized by means of photo and electroluminescence images of wafers and solar cells from different heights. At these locations, detailed measurements of the crystal structures and orientations allowed the following conclusions.

All three defect clusters formed in similar crystal configura tions, even though they had been chosen by their size only. Each of the clusters seems to start close to a large grain boundary. It could be shown with EBSD measurements that all these boundaries consist of Σ9 and Σ27 boundaries, forming the boundaries of (111) grains on one side and twinned (101) grains on the other side. The clusters always formed inside the (101) grains. One of the clusters started to grow already close to the bottom of the ingot. For another cluster, signs of crystal deformations near the cluster's

origin as well as Raman measurements indicate stresses that might lead to the cluster formations. Additionally, the vertical disappearing of a cluster during crystallization at a grain boundary shows the same crystal configurations as for the growing clusters. In this case, the cluster approaches the (101)/(111) grain boundary while the growing clusters shift away.

Further experiments on other multicrystalline silicon materials need to be carried out to clarify if the results presented here are limited to the investigated material or are generally valid.

Acknowledgments

The financial support from the BMU project FKZ 0325581 is gratefully acknowledged in particular for the characterization equipment. The content of this publication is the responsibility of the authors.

References

[1] B.L. Sopori, Defect clusters in silicon: impact on the performance of large-area devices, Materials Science Forum 258–263 (1997) 527–534.
[2] B. Sopori, P. Rupnowski, V. Mehta, V. Budhraja, S. Johnston, N. Call, H. Moutinho, D. Carlson, and M. Al-Jassim, Defect clusters in multicrystalline silicon: their nature and influence on the solar cell performance, in: Proceedings of the 34th IEEE Photovoltaic Specialists Conference (PVSC), 2009 pp. 1969–1974.
[3] M.M. Kivambe, G. Stokkan, T. Ervik, B. Ryningen, O. Lohne, The microstructure of dislocation clusters in industrial directionally solidified multicrystalline silicon, Journal of Applied Physics 110 (6) (2011) 063524.
[4] S. Martinuzzi, I. Périchaud, F. Warchol, Hydrogen passivation of defects in multicrystalline silicon solar cells, Solar Energy Materials and Solar Cells 80 (3) (2003) 343–353.
[5] C. Donolato, Modeling the effect of dislocations on the minority carrier diffusion length of a semiconductor, Journal of Applied Physics 84 (5) (1998) 2656–2664.
[6] T. Kieliba, S. Riepe, W. Warta, Effect of dislocations on open circuit voltage in crystalline silicon solar cells, Journal of Applied Physics 100 (9) (2006) 93708.
[7] D. Kohler, D. Kiliani, B. Raabe, S. Seren, and G. Hahn, Comparison of UMG materials: are ingot height independent solar cell efficiencies possible? in: Proceedings of the 25th EU PVSEC, 2010 pp. 2542–2547.
[8] J. Haunschild, M. Glatthaar, M. Demant, J. Nievendick, M. Motzko, S. Rein, E.R. Weber, Quality control of as-cut multicrystalline silicon wafers using photoluminescence imaging for solar cell production, Solar Energy Materials and Solar Cells 94 (12) (2010) 2007–2012.
[9] C. Häßler, G. Stollwerck, W. Koch, W. Krumbe, A. Müller, D. Franke, T. Rettelbach, Multicrystalline silicon for solar cells: process development by numerical simulation, Advanced Materials 23 (2001) 1815–1819.
[10] N. Usami, R. Yokoyama, I. Takahashi, K. Kutsukake, K. Fujiwara, K. Nakajima, Relationship between grain boundary structures in Si multicrystals and generation of dislocations during crystal growth, Journal of Applied Physics 107 (1) (2010) 013511.
[11] K. Hartman, M. Bertoni, J. Serdy, T. Buonassisi, Dislocation density reduction in multicrystalline silicon solar cell material by high temperature annealing, Applied Physics Letters 93 (12) (2008) 122108.
[12] M. Di Sabatino, G. Stokkan, Defect generation, advanced crystallization, and characterization methods for high-quality solar-cell silicon, Physica Status Solidi A 8 (2012) 1–8.
[13] C. Häßler, E.-U. Reisner, W. Koch, A. Müller, D. Franke, T. Rettelbach, low dislocation density multicrystalline silicon for photovoltaic applications, Solid State Phenomena 67–68 (1999) 447–452.
[14] D. Franke, T. Rettelbach, C. Häßler, W. Koch, A. Müller, Silicon ingot casting: process development by numerical simulations, Solar Energy Materials and Solar Cells 72 (2002) 83–92.
[15] F. Secco d'Aragona, Dislocation etch for (100) planes in silicon, Journal of The Electrochemical Society 119 (7) (1972) 948–951.
[16] G.E. Lloyd, Atomic number and crystallographic contrast images with the SEM: a review of backscattered electron techniques, Mineralogical Magazine 51 (1987) 3–19.
[17] A. Zuschlag, H. Morhenn, J. Bernhard, J. Junge, S. Seren, and G. Hahn, Microscopic analysis of the influence of solar cell process steps on the recombination activity of extended crystal defects, in: Proceedings of the 25th EU PVSEC, 2010, pp. 2433–2437.
[18] D. Kohler, S. Braun, B. Raabe, S. Seren, G. Hahn, Upgraded metallurgical grade silicon solar cells: A detailed material analysis, in: Proceedings of the 25th EU PVSEC, 2009, pp. 1758–1761.
[19] R. Kopecek, J. Arumughan, K. Peter, E.A. Good, J. Libal, M. Acciarri and S. Binetti, Crystalline Si solar cells from compensated material: behaviour of light induced degradation, in: Proceedings of the 25th EU PVSEC, 2008, pp. 1855–1858.
[20] K. Fujiwara, K. Maeda, N. Usami, G. Sazaki, Y. Nose, K. Nakajima, Formation mechanism of parallel twins related to Si-facetted dendrite growth, Scripta Materialia 57 (2) (2007) 81–84.
[21] D. Hull, D.J. Bacon, Introduction to Dislocations, 5th ed., Elsevier Ltd., 2011.
[22] B. Ryningen, G. Stokkan, M. Kivambe, T. Ervik, O. Lohne, Growth of dislocation clusters during directional solidification of multicrystalline silicon ingots, Acta Materialia 59 (20) (2011) 7703–7710.
[23] I. Odland and G. Stokkan, Mechanisms for formation of dislocations near the bottom of a multicrystalline silicon ingot, in: Proceedings of the 4th International Workshop on Crystalline Silicon Solar Cells (CSSC 4), 2010 pp. 3–5.
[24] T. Maitland, S. Sitzman, in: W. Zhou, Z.L. Wang (Eds.), Electron Backscatter Diffraction (EBSD) Technique and materials characterization examples, in Scanning Microscopy for Nanotechnology: Techniques and Applications, 1st ed.,Springer, New York, 2007, pp. 41–75.
[25] J. Zhao, B.L. Adams, Definition of an asymmetric domain for intercrystalline misorientation in cubic materials in the space of Euler angles, Acta Crystallographica Section A: Foundations of Crystallography 44 (3) (1988) 326–336.
[26] P. Taylor, A. Garg, W.A.T. Clark, J.P. Hirth, Dissociated and faceted large-angle coincident-site-lattice boundaries in silicon, Philosphical Magazine A 59 (3) (1989) 479–499.
[27] T. Ervik, M. Kivambe, G. Stokkan, B. Ryningen, and O. Lohne, Dislocation formation at Σ 27a boundaries in multicrystalline silicon for solar cells, in: Proceedings of the 25th EU PVSEC, 2011, pp. 1895–1899.
[28] B. Ryningen, Formation and growth of crystal defects in directionally solidified multicrystalline silicon for solar cells (Ph.D. thesis), NTNU Trondheim, 2008.
[29] K. Fujiwara, Y. Obinata, T. Ujihara, N. Usami, G. Sazaki, K. Nakajima, Grain growth behaviors of polycrystalline silicon during melt growth processes, Journal of Crystal Growth 266 (4) (2004) 441–448.
[30] K. Fujiwara, K. Nakajima, T. Ujihara, N. Usami, G. Sazaki, H. Hasegawa, S. Mizoguchi, K. Nakajima, In situ observations of crystal growth behavior of silicon melt, Journal of Crystal Growth 243 (2) (2002) 275–282.